

Plasma electrolytic oxidation thermal barrier coating for reduced heat losses in IC engines

Abdelrahman Hegab ^{a,*}, Kamal Dahuwa ^a, Reza Islam ^a, Alasdair Cairns ^a, Ankit Khurana ^b, Suman Shrestha ^b, Robin Francis ^b.

^a *Department of Mechanical, Materials and Manufacturing Engineering, University of Nottingham, Nottingham NG7 2RD, UK*

^b *Keronite International Ltd, Haverhill CB9 8PJ, UK*

*Corresponding author. Tel.: +44 115 82 32595; E-mail address: Abdelrahman.Hegab@nottingham.ac.uk

Abstract

The work involved the development and on-engine testing of a new “thermo-swing” barrier coating for reduced wall heat transfer and increased thermal efficiency in future diesel engines utilizing aluminium alloy pistons. Such swing coatings, of low thermal conductivity and low specific heat capacity, have recently been proposed to produce a dynamic thermal barrier layer that rapidly changes the temperature of the upper surface of the piston crown in response to the adjacent in-cylinder gas temperature. The new coating tested in this work was formed directly from the piston substrate material using an optimised plasma electrolytic oxidation process, with a silica top coat subsequently applied to entrap air within coating pores. Benchtop laser flash measurements were undertaken to quantify coating thermal properties and provide the required empirical data for future thermal simulation. Coatings of varying features were tested in a bespoke thermodynamic single cylinder diesel engine instrumented for precision measurements of in-cylinder pressure, fuel

consumption and legislated engine-out emissions. The optimum coating applied across the full piston crown and bowl enabled up to 3% improvement in indicated thermal efficiency under idealised part load operating conditions. The coating reduced heat transfer during combustion, leading to elevated engine-out NO_x. By retarding combustion phasing slightly from the optimum, the NO_x increase could be mitigated while still retaining most of the fuel consumption benefit, with the remaining benefit associated with reduced heat transfer during the remaining power stroke. The emissions of other key pollutants (CO, unburned hydrocarbons and soot) were less affected under the part load conditions tested.

Keywords

Thermal barrier coating; Thermo-swing; Plasma electrolytic oxidation; Heat loss reduction; Engine thermal efficiency

Abbreviations

AFR, air-to-fuel ratio; ANO, anodised; ATDC, after top dead centre; BSFC, brake specific fuel consumption; BSLN, baseline; BTE, brake thermal efficiency; CA, crank angle; CNHR, cumulative net heat release; CO, carbon monoxide; CR; compression ratio; DI, direct Injection; ECU, engine control unit; EGR, exhaust gas recirculation; EXP, exhaust manifold pressure; FE, fuel energy; FSN, filter smoke number; GHG, greenhouse gas, HPCR, high-pressure common-rail; HRR, heat release rate; IC, internal combustion; IMEP, indicated mean effective pressure; LFA, laser flash analyzer; LHV, lower heating value; MAP, manifold absolute pressure; NO_x, nitrogen oxides; PEO, plasma electrolytic oxidation; ROPR, rate of pressure rise; SEM, Scanning Electron Microscopy; SiRPA, Silica reinforced porous anodised aluminum; SOC, start of combustion; SOI, start of injection; TBC, thermal barrier coating, TDC, top dead centre; THC, total hydrocarbon; TSWIN, Thermo-swing wall insulation technology; YSZ, yttria stabilized zirconia.

1 Introduction

Climate change and local air quality must both be addressed at an accelerated rate. Transport is the second largest greenhouse gas (GHG) emitting sector globally, and accounts for 27% of total GHG emissions in the UK, where 91% of these come from road transport [1]. Global concern regarding vehicle emissions has notably escalated in recent years, and major cities around the world, including Paris, Madrid, Mexico City, and Athens have declared their intentions to ban diesel vehicles from city centres by 2025 [2]. In early 2020, the UK government announced an aggressive stance and stated that the sales of new petrol, diesel and (potentially) hybrid cars will be banned from 2035, five years earlier than initially planned, in an attempt to reduce air pollution and attain net zero-emissions by 2050 [3]. While the global electric car fleet has almost doubled in number over the past two years with more significant growth to come [4], electric vehicles still only represent a small percentage of vehicles sales, and issues over charging infrastructure, customer acceptance and battery supply may mean that complete conversion takes decades [4]. Furthermore, the electrification of transport currently primarily targets passenger cars, and internal combustion (IC) engines are projected to remain in wide use beyond 2040 in heavy duty applications (road, rail, marine, power generation and hybrids) [5]. As the transition to the use of low-carbon fuels and hybridization in heavy duty transport is regarded as a medium-term strategy to approach a more sustainable transport, efforts to develop more energy-efficient and eco-friendly IC engines must continue [6]. In recent years, there has been a notable work to develop innovative combustion systems that improve the NO_x-soot tradeoff, while offering a higher engine specific power [7]. Examples include the development of advanced piezo fuel injection system (FIS) that can produce injection pressures as high as 3000 bar [8], and the use of additive manufacturing to create innovative piston bowl with complex geometry that cannot be produced by standard manufacturing technologies [9].

In line with recent innovation and technologies to improve engine efficiency, research efforts on engine thermal management remain pivotal. One fundamental way to develop high efficiently IC engines is to reduce the losses associated with the process of converting the fuel chemical energy into useful work. Typical modern automotive diesel engines reject about 60% of the fuel energy as a waste heat, mainly to the coolant and to the exhaust gas, in roughly equal shares [10]. For combustion of a given mass of fuel inside the engine cylinder, higher heat transfer to the combustion chamber walls will lower the average gas temperature and pressure; reducing the work per cycle transferred to the piston and hindering complete fuel oxidation [11]. In an attempt to overcome this, the concept of adopting thermal barrier coatings (TBC) has been employed in IC engines since the 1980s [12], in which typically a ceramic-based material coating of low thermal conductivity is applied to the whole combustion chamber surface, or to certain parts such as the piston crown, cylinder head, liner or valves [13]. The target is to insulate the heat flow from the working gas to the combustion cylinder wall by keeping the wall surface at high temperature or reducing local material thermal conductivity during the combustion process, hence reducing the heat loss to the coolant [14]. Some of the additional heat energy that has become available in the engine cylinder would then be converted to useful work output; improving engine thermal efficiency and reducing the brake specific fuel consumption (BSFC) [15]. Reducing the heat transfer also increases the exhaust gas temperatures, which provides greater potential for energy recovery through the use of, for example, electric turbo-compounding or thermoelectric generators [16]. Additional benefits include the protection of combustion chamber components from thermal stresses and reduced cooling requirements, where a simpler cooling system would reduce the weight and cost of the engine while improving reliability [15], and faster catalytic light-off for reduction of harmful emissions following cold start [17], which may become a key priority in future hybrid (and potentially geo-fenced) trucks. Recent works also investigated insulating the exhaust manifold, which has been found to improve both trade-offs; NO_x-Soot and NO_x-BSFC in modern truck engines [18].

Several ceramic materials have been used for TBC applications over the years, with different processing techniques for coating deposition investigated [19]. Currently, one of the most popular and widely used TBC materials is Ytria Stabilized Zirconia (YSZ) as it provides the best performance in high temperature zones [20]. Nevertheless, traditional ceramic coating insulation technology keeps the wall temperature at high levels even during the intake and compression strokes, due to the large heat capacity of the coating material [21]. Inevitably, engine volumetric efficiency decreases and the working gas temperature increases, which leads to lower work output and worsened emissions characteristics [22]. The ignition delay becomes shorter, resulting in more diffusion combustion and slower mixture formation in diesel engines. Elevated intake temperature also increases the likelihood of end-gas auto-ignition and knock in spark ignition engines [23].

In recent years, some investigations have shown through both simulations and experiments the effectiveness of thin ceramic coatings with low-thermal-conductivity on performance and emissions of spark ignition, diesel and homogeneous charge compression ignition engines [24-26]. The thin coatings improve fuel economy without large penalty on the volumetric efficiency. However, a breakthrough in TBC technologies was the recently reported development of Toyota Silica Reinforced Porous Anodised Aluminum (SiRPA) coating [27]. In this technology, known as Thermo-Swing Wall Insulation Technology (TSWIN), the coating material has the capacity to rapidly change the wall temperature in a more dynamic way to follow the transient gas temperature [28]. This was attributed to the low-thermal-conductivity and low-heat-capacity of the TSWIN coating, which causes its surface temperature to change greatly even during an extremely short cycle time [29]. A comparison of conventional aluminum piston temperature, traditional TBCs and Thermo-Swing coating through a cycle relative to gas temperature is shown in Figure 1 [21]. It can be seen from the figure that the surface temperature with Thermo-Swing coating increases during the combustion period, and decreases during the exhaust and intake strokes; dynamically with the gas temperature.

This decreases the heat loss (compared to a conventional uncoated piston) and prevents the intake air heating encountered with traditional TBC coatings.

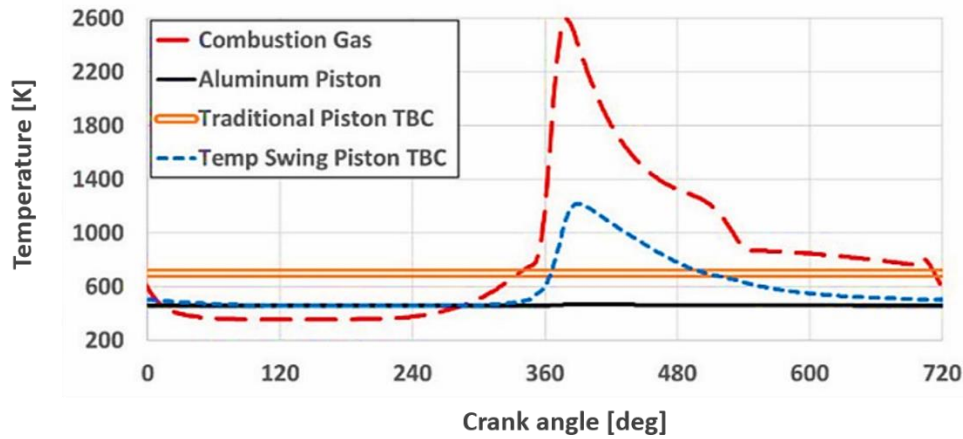


Figure 1 Comparison of conventional aluminum piston, traditional TBC and thermos-swing coating temperature relative to gas temperature. Adapted from Ref. [21].

Nevertheless, the high surface roughness that is typical for anodised TBCs, including TSWIN, was found to increase heat transfer, slow down combustion and increase THC emissions [30].

Undesirable interaction between the fuel spray and the coating surface roughness was encountered in the diesel piston bowl area, which led to the adoption of the coating on the squish-region of the piston only [31]. In addition to the high surface roughness, porosities and imperfection of the coating process, including non-uniformity of coating thickness, limited the benefits of the TSWIN coating to some extent. The nano pores at the bottom part of the insulation layer could harbor some of the high-temperature and high-pressure in-cylinder gas during the combustion period, which deteriorates the insulation performance [23]. This was counteracted by the use of silica sealant, although this added an unwanted additional layer to the optimum coating thickness [32].

One innovative surface coating technique that overcomes many of these problems is Plasma Electrolytic Oxidation (PEO) [33], which is a high voltage process that offers attractive combinations

of hardness, wear resistance, corrosion resistance and interfacial adhesion [34]. PEO creates thin coatings with ultra-low thermal conductivity and heat capacity, with improved homogeneity in coating thickness, porosity and high surface finish [35]. In the PEO process, the coating grows both inward to the alloy substrate and outward to the coating surface simultaneously which results in excellent adhesion to the substrate metal [36]. The microstructural characteristics of PEO coatings depend on operational conditions (e.g. voltage level, process duration and electrolyte composition), which can be tailored in accordance with the desired thermal properties, porosity and thickness [37]. These merits give PEO advantages over more conventional coating techniques, and hence PEO has penetrated specialist markets in surface engineering, including automotive engines and many other industrial applications, yet still subjected to further development [38].

The aim of the currently reported work has been to experimentally investigate the potential benefits of applying a novel PEO coating to a diesel engine piston, with focus upon impact on reducing wall heat transfer losses in the engine to improve thermal performance and hence overall engine thermal efficiency. The work incorporated development of the piston coating, where the main objectives were to produce a thin layer coating of low specific heat capacity and low thermal conductivity. Detailed comparative results between a standard uncoated piston, PEO coated piston and traditional anodised (ANO) piston are presented including engine combustion pressure and Heat Release Rates (HRR), thermal efficiency, NO_x, soot, CO and Total Hydrocarbon (THC) emissions.

2 Experimental Approach

The experimental work carried out comprised the development of the thermal barrier coating that had been applied to the engine piston, followed by testing the engine combustion, performance and emissions using different piston coatings. This section serves to describe the processes of preparing

the piston coatings, examining its microstructure and measuring its thermal properties. Engine test facility, data acquisition system and test program are then described.

2.1 Piston coating development

2.1.1 Plasma electrolytic oxidation coating

Coatings were prepared using a 25 kW Keronite processing rig and an electrolyte consisting of a dilute alkaline electrolyte containing sodium silicate (10-20 g/L concentration) and potassium hydroxide (1-2 g/L concentration). The electrolyte was maintained at a temperature of approximately 15°C by re-circulation through a heat exchanger and a bipolar waveform was applied. The approximate current density was 10 A/dm². Voltages applied were ~450V anodic and ~150V cathodic. The coatings were applied to the top face of Ford Puma series diesel pistons supplied by Federal Mogul/Tenneco. The piston material was a cast aluminum containing ~12-14% silicon. The pistons were approximately 80 mm in diameter. Initial development and characterization of the coatings was performed on coupons of 5 cm diameter as described further in section 3.1.1. Following processing the parts were thoroughly rinsed with de-ionised water. In some cases, a high silicate sealer was applied to the top surface post coating using a spray gun. The sealer thickness above the PEO layer was ~2-5 µm. Some penetration of the sealer into the top porous section of the PEO coating was noted.

The PEO coating was applied to the entire top face of the piston. The counter electrode was a steel cage surrounding the processing tank which was ~100 L in volume. The distance between the piston crown and counter electrode was approximately 10 cm. The coating process was continued until the coating thickness on the crown surface (the top outer ring) was 65-70 µm. Coating time was ~20 mins. Generally even growth was seen, although the coating was somewhat thinner (30-40 µm) in the bowl area underneath the crown lip. Coating thicknesses during and after processing were assessed using Eddy Current Testing. These measurements were double checked by sectioning

coated parts and examining the coating thickness in cross-section using optical microscopy and Scanning Electron Microscopy (SEM).

The resulting coatings comprise a mixture of alumina (α and γ phases) and silicate phases such as mullite ($3\text{Al}_2\text{O}_3 \cdot 2\text{SiO}_2$). Composition measurements using SEM suggest approximately equal proportions of mullite and alumina.

2.1.2 Optical and electron microscopy

Coating surface morphology and microstructure were analyzed by using a Leica MZ6 optical microscope for low magnification up to 4 times, and a Nikon Eclipse L150 up to 1000 times.

Scanning electron microscopy analysis was performed using a Cambridge Instruments SteroScan 240 scanning electron microscope.

2.1.3 Thermal property measurements

Thermal properties were measured on a Netzsch Laser Flash Analyzer (LFA) 457 instrument which gives a direct measurement of the thermal diffusivity of a sample by measuring the temperature rise on the back side of a sample after being exposed to a light flash on the front side. Circular coupons of 12.7mm diameter and ~3mm thickness were used for the thermal property measurements. These were coated and sealed on one side, and finally coated in a thin layer of graphite to ensure absorption of the shots. Three measurements were taken at each temperature.

A two-layer model was used to convert the thermal diffusivity value to a thermal conductivity of the coating using the integrated software within the LFA 457 instrument. Relevant materials input parameters for the model are the density, coefficient of thermal expansion, and heat capacities as a function of temperature for both coating and substrate, and the coating thickness. These parameters were known from previous work. For the alloy, inputs were a density of 2.8 g/cm^3 , a coefficient of thermal expansion of $19 \text{ } \mu\text{m/m.K}$, and a specific heat capacity (room temperature) of 750 J/kg.K . For

the coating, inputs were a density of 1.9 g/cm^3 , a coefficient of thermal expansion of $4 \text{ }\mu\text{m/m.K}$, and a specific heat capacity (room temperature) of 800 J/kg.K . Coating thickness was $70 \text{ }\mu\text{m}$. Further details of the application of the flash method using the LFA 457 instrument and the process for calculating the thermal conductivity of samples have been published by Netzsch [39].

2.2 Experimental Setup

2.2.1 Engine test facility

The experiments were carried out on a Ricardo Hydra, single cylinder, 0.55 litre Direct Injection (DI) diesel engine, with the cylinder head, piston assembly and controls adapted from a Ford Puma 2.2 litre production engine. The engine was equipped with a high-pressure common-rail (HPCR) fuel injection system, including an 8 hole centrally mounted piezo-electric injector, offering up to 6 injections per cycle at a pressure of up to 2000 bar. The engine intake system was fitted with an air plenum to moderate the pulsation effect resulting from the engine suction, electric air heater, air throttle and external Exhaust Gas Recirculation (EGR) loop (albeit fully closed off throughout). The main specifications of the engine are listed in Table 1. A schematic diagram of the experimental setup is shown in Figure 2.

The engine was connected to a David McClure swinging frame DC dynamometer with a rated capacity of 60 kW at 4500 rpm. The dynamometer was controlled using a Control Techniques Mentor II DC drive unit capable of motoring and absorbing operation to maintain a steady speed against varying engine torque throughout the cycle.

Table 1 Main specifications of the test engine

<i>Model</i>	<i>Ricardo Hydra</i>
No. of cylinders	1
Capacity	0.55 litre
Cooling system	Water cooled
Induction system	Naturally aspirated
EGR system	Electronically controlled External loop
Bore	86.0 mm
Stroke	94.6 mm
Compression ratio	15.5:1
Fuel injection system	High-pressure common-rail (HPCR)
Common rail pressure	Up to 2000 bar
Valves per cylinder	2 intake; 2 exhaust

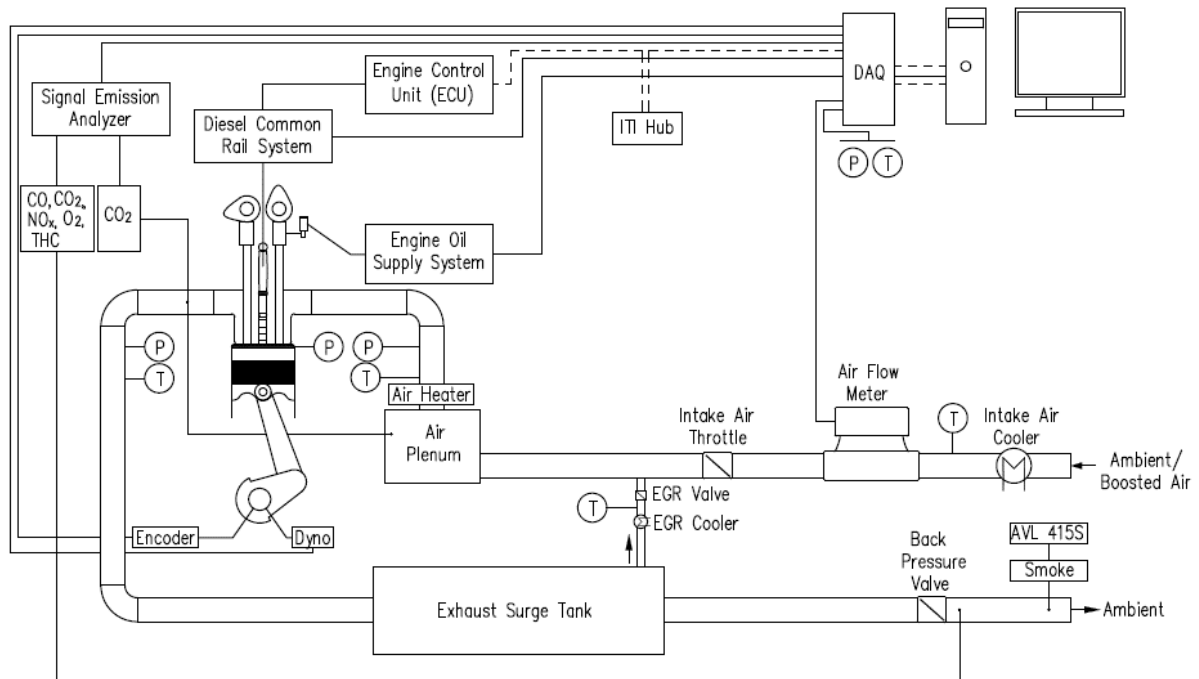


Figure 2 A Schematic diagram of the experimental setup.

2.2.2 Data acquisition and instrumentations

All experimental data was captured in a desktop PC via an integral data acquisition system and control programs. Engine operating parameters were monitored and controlled through the Engine

Control Unit (ECU). The ECU was connected through a network hub to the PC, where the engine management software was installed and used to communicate with the ECU. The software interface provided control of various injection parameters such as injection quantity, injection timing (and therefore separation), number of injections and rail pressure. Diesel fuel flow rate was also measured by a set of two micro-motion Coriolis mass flow sensors, model CFMS015M by Emerson, fitted in the fuel supply and return lines. Engine torque was measured using a load cell, model KIS-3 by BLH Nobel, attached to the dynamometer. Engine speed and crankshaft position were monitored using a Hohner W2D11R incremental optical shaft encoder, with an accuracy of 0.5 degree. The in-cylinder pressure was measured using Kistler 6055C piezoelectric non-cooled combustion pressure sensors fitted into the cylinder head glow plug hole that has been deactivated. The output signal of the pressure transducer was fed to a dedicated Kistler 5011 charge amplifier, comprising a high-gain inverting voltage amplifier with a MOSFET input for high insulation resistance. In-cylinder pressure and crank position signals were fed into high-speed National Instruments (NI) modules NI 9220 and NI 9401, respectively, mounted on a cDAQ-9178 CompactDAQ chassis, to obtain the crank angle-synchronized in-cylinder pressure data in LabVIEW environment. Type-K thermocouples were fitted throughout to measure the coolant temperatures, oil temperatures, intake and exhaust manifolds temperatures, and fuel lines temperatures. The output signals were acquired using a NI-9213 thermocouple module mounted on the cDAQ chassis. A set of Kulite PT-2054 non-amplified pressure sensors and Kulite PT-2028 amplified pressure sensors were used to measure oil pressure, intake Manifold Absolute Pressure (MAP), and Exhaust Manifold Pressure (EXP). Exhaust gas emissions (THC, CO, CO₂ and NO_x), and O₂ concentration were measured using a Signal gas analyzer system, while the Filter Smoke Number (FSN) was measured using an AVL filter-type smoke meter, model 415S. The output analogue signals were acquired using a NI-9205 module mounted on the cDAQ chassis, and then read in LabVIEW environment. The uncertainties of the main measured parameters are summarised in Table 2.

Table 2 **Uncertainties of the main measured parameters**

<i>Measured parameter</i>	<i>Uncertainty (%)</i>
Diesel fuel flow rate	0.86
Torque	1.05
In-cylinder pressure	0.62
Manifold pressure	0.68
THC emissions	1.57
CO emissions	5.92
NOx emissions	2.34
Soot emissions	3.10

2.2.3 Test conditions and procedure

The focus of this study has been the part load conditions that prevail in modern city traffic. Tests were conducted at different engine speeds, ranging from 750 (idling) to 2000 rpm, at load sweep varying from 2.1 to 5.1 bar net Indicated Mean Effective Pressure (IMEP_n). Diesel fuel injection was split into a fixed mass pilot injection of 1mg/stroke, followed by the main injection of a varying mass according to the engine load. The test matrix of the main engine parameters investigated is summarised in Table 3. The different combinations of fuel injection timing used are outlined in Table 4, for an easier referring henceforth.

Table 3 **Test matrix of main engine parameters**

<i>Parameter</i>	<i>Value</i>
Engine speed (rpm)	750, 1250, 1500, 2000
IMEP _n (bar)	2.1, 3.4, 3.8, 5.1
Fuel rail pressure (bar)	600
Injection pattern	Double injection (pilot + main) with 15° CA spacing
SOI; pilot (° CA ATDC)	-25, -20, -15, -10, -5
SOI; main (° CA ATDC)	-10, -5, 0, 5, 10
Injection mass; pilot (mg/st)	1
Injection mass; main (mg/st)	Varies according to the load
Combustion phasing; CA50	Varies with the injection timing
Boost level	N/A
EGR	0
Intake air temperature (° C)	40

Table 4 Fuel injection timing combinations

<i>Case</i>	<i>Pilot injection timing; SOI (°CA ATDC)</i>	<i>Main injection timing; SOI (°CA ATDC)</i>
Timing A	-25	-10
Timing B	-20	-5
Timing C	-15	0
Timing D	-10	5
Timing E	-5	10

For each test case examined, the variation of cylinder pressure with crank angle position was recorded for 300 consecutive cycles, and the ensemble average of these 300 combustion cycles was then filtered to remove any noise spikes, then processed for further calculations. The net heat release rate (HRR) was calculated using the well-known first law equation [10]:

$$\frac{dQ_{net}}{d\theta} = \frac{\gamma}{\gamma-1} p \frac{dV}{d\theta} + \frac{1}{\gamma-1} V \frac{dp}{d\theta} \quad (1)$$

where (θ) is the crank angle, (p) is the in-cylinder pressure at a given crank angle, (V) is the cylinder volume at that point, and (γ) is the specific heat ratio (C_p/C_v), calculated from a polynomial function of bulk gas temperature at the corresponding crank angle [40]. Integrating the HRR as a function of crank angle provides a representation of the total energy released up to a specified angle (aka cumulative heat release). The crank angle at which 50% of heat release occurs (CA50) is used to present combustion phasing [41], and it characteristically changed with the injection timing. Net indicated mean effective pressure is identified as the work transferred to the piston from the gas over the entire four-stroke cycle, per unit unit displaced volume [10];

$$IMEP_n = \frac{\oint p dV}{V_{disp}} \quad (2)$$

If the integration is carried out over the compression and expansion strokes only, the work developed is referred to as the gross indicated work, and the output of Eq. (2) is called “Gross Indicated Mean

Effective Pressure” (IMEP_g). Gross indicated thermal efficiency is used to indicate how well the fuel is being utilised and transferred to useful work, and identified as [10]:

$$\eta_{ind,g} = \frac{IMEP_g \times V_{disp}}{m_f \times LHV_f} \quad (3)$$

where (m_f) is the fuel mass injected per cycle; (mg), and (LHV_f) is the lower heating value of fuel; (MJ/kg). A value of $LHV_f = 42.5$ MJ/kg is used in this study [10].

Engine energy balance is calculated by applying the first law of thermodynamics to the control volume surrounding engine [10]. When no EGR is used, a steady-flow energy conversion equation may be expressed as [42]:

$$P_b = \dot{m}_f LHV_f - P_f - P_p - \dot{Q}_{HT} - \dot{Q}_{Exh} - \dot{Q}_{l,comb} \quad (4)$$

where (P_b), (P_f) and (P_p) are the brake power, mechanical friction and pumping power losses, respectively, ($\dot{Q}_{l,HT}$), ($\dot{Q}_{l,Exh}$) and ($\dot{Q}_{l,comb}$) are the thermal energy losses due to heat transfer, exhaust gas and combustion inefficiency, respectively.

By definition, gross indicated work represents the sum of the useful work available at the shaft and the work required to overcome engine losses in mechanical friction and pumping work [10]; i.e.:

$$P_{i,g} = P_b + P_f + P_p \quad (5)$$

Engine energy balance may, therefore, be expressed as:

$$P_{i,g} = \dot{m}_f LHV_f - \dot{Q}_{HT} - \dot{Q}_{Exh} - \dot{Q}_{l,comb} \quad (6)$$

For naturally aspirated engine where the exhaust gas is discharged from the cylinder directly to the ambient, exhaust gas heat loss can be expressed as:

$$\dot{Q}_{Exh} = (\dot{m}_a + \dot{m}_f) \cdot c_{p_{Exh}} \cdot (T_{Exh} - T_{Amb}) \quad (7)$$

where (\dot{m}_a) is the mass flow rate of air, ($c_{p_{Exh}}$) is the specific heat of the exhaust gas; (J/kg.k), calculated at its temperature as it leaves the engine (T_{Exh}) [10], and (T_{Amb}) is ambient temperature.

Combustion losses are calculated from the measured concentrations of the combustible products in the exhaust gas [10], as:

$$\dot{Q}_{l,comb} = \frac{\sum_i x_i \cdot LHV_i}{[\dot{m}_f/(\dot{m}_a + \dot{m}_f)] \cdot LHV_f} \quad (8)$$

where (x_i) is the mass fraction of any combustible product on the exhaust gas (CO, THC, and soot), and (LHV_i) is the lower heating value of the particular species.

Applying Eq. (6), it becomes possible to calculate the heat transfer losses (\dot{Q}_{HT}) knowing the other parameters [42].

Engine tests were carried out using four different types of pistons; the standard uncoated piston that has been used as a baseline for comparison, two PEO coated pistons with different coating forms and one ANO coated piston. The four pistons used in the tests are identified in Table 5. Set out in Figure 3 are photographs of the pistons used.

Table 5 Summary of different pistons used

<i>Piston designation</i>	<i>Description</i>
BSLN	Baseline, standard uncoated piston as supplied by the manufacturer
PEO1	PEO crown-and-bowl coated piston, sealed, extra-smooth bowl, coating thickness 70 μm
PEO4	PEO crown-and-bowl coated piston, sealed, coating thickness 70 μm
ANO1	ANO crown coated piston, coating thickness 50 μm , no sealant



Figure 3 Photographs of the typical pistons used in the present study.

The baseline testing was repeated after each engine rebuild to ensure there was no drift. Cylinder head height relative to the piston was adjusted after every rebuild using a series of shims, in order to maintain the geometric compression ratio (CR) within ± 0.01 with different piston coating thicknesses.

All tests were undertaken at fully warm engine conditions. The engine coolant temperature was kept at $90^{\circ} \pm 2^{\circ}\text{C}$. The external EGR loop was deactivated so that the effects of piston coating were not masked by the variation of EGR rates. Nevertheless, the intake air temperature was maintained at $40^{\circ} \pm 1^{\circ}\text{C}$ to emulate the temperature effect of the EGR that would be encountered in real driving conditions [43].

Due to space limitation, only results for engine testing at 1500 rpm and 3.8 bar IMEP_n are presented; other results exhibited fairly similar trends.

3 Results and discussion

3.1 Microstructural and thermal property investigation

3.1.1 Coupon preparation and microstructure

A thermal swing coating should have as low a thermal conductivity and volumetric heat capacity as possible, ideally $< 1 \text{ W/mK}$ and $< 1,500 \text{ kJ/K/m}^3$ respectively. However, for practical application further properties are needed, namely excellent adhesion to the substrate, durability under conditions found in-cylinder, and low surface roughness such as not to interfere with combustion.

Keronite's PEO coating process converts the surface of aluminum parts to a ceramic layer, mainly comprising the alpha and gamma phases of alumina [34]. However, other species such as silicate can be incorporated from the electrolyte. Since the PEO layer is formed at least partially via conversion of the substrate, adhesion is extremely good (no significant detachment using industry standard scratch adhesion tests such as ASTM D3359) [35] and the tolerance of PEO layers to thermal cycling is excellent [44]. PEO layers are inherently porous due to the nature of the process [33].

While the thermal conductivity of alumina is significantly lower than aluminum at $\sim 30 \text{ W/mK}$, this is still considerably above the target of 1 W/mK . Incorporation of other very low thermal conductivity phases such as mullite, an aluminosilicate with a thermal conductivity of $\sim 2\text{-}4 \text{ W/mK}$, is therefore advantageous. Furthermore, since air has both a low thermal conductivity and heat capacity, maximizing porosity is a critical element of developing thermal swing coating. However, highly porous coatings tend to be rougher which may have negative impacts on combustion [45], so it is important to maximize porosity while minimizing the effect on surface roughness. Keronite has specifically engineered its thermal swing coatings to contain high quantities of low thermal conductivity phases such as mullite, and to be highly porous, yet smooth ($R_a < 3 \text{ }\mu\text{m}$ as coated, $< 1 \text{ }\mu\text{m}$ for sealed samples) [44].

Initial development and characterization of the coatings was performed on coupons of 5 cm diameter, made from an alloy chosen to be similar to that of typical piston alloys. The alloy has a nominal composition of 12-14% Si, 3-4% Cu, 2.8-3.0% Ni, 0.5-1% Mg, Balance Al. A number of variants of electrolyte (different concentrations of sodium silicate and potassium hydroxide) and electrical regime (applied voltage) were investigated to optimize the coatings. The selected optimal coating had a nominal thickness of 65-70 μm and surface roughness (Ra) of ca. 2.7-3.0 μm . The visual appearance of the coatings is shown in Figure 4.



Figure 4 Representative coupons coated with Keronite's thermal swing coating

The free surface and cross sections of coated samples were examined by visual microscopy and SEM. Figure 5(a) is a SEM micrograph of the free surface (top view), while Figure 5(b) is SEM micrograph of a cross section. The samples were sputtered with gold prior to imaging, but otherwise no other special preparation steps were performed. Significant porosity is evident which appears to be largely open, including down to the substrate interface in at least some areas. The coating and pore structure were highly uniform across the samples. Some samples were additionally sealed with a perhydropolysilazane sealer. A free surface micrograph of the surface post sealing is shown in Figure 5(c). Some cracking of the surface is evident, but the sealer layer was well adhered with the PEO layer. A slightly tilted cross section of a sealed sample is shown in figure 5(d). It can be seen that the sealer forms a thin blanket over the coating. However, some sealer is also seen to penetrate the top section of the coating.

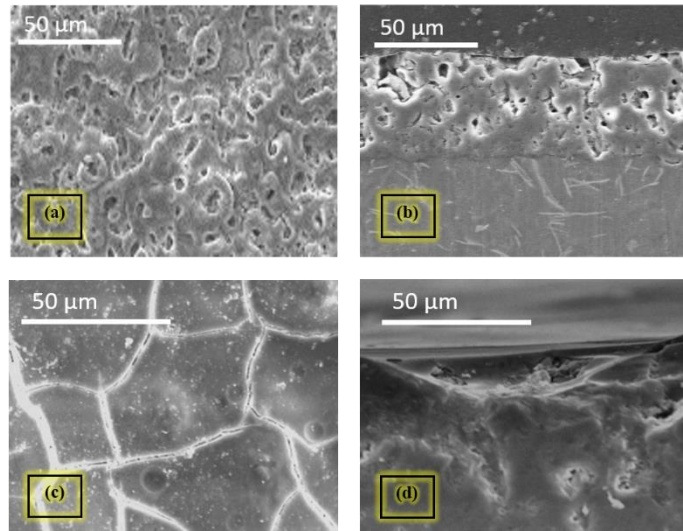


Figure 5 (a) Free surface SEM of the PEO surface, (b) cross-sectional SEM of the PEO coating, (c) free surface SEM of the PEO coating after application of the sealer, and (d) slightly tilted cross section of a sealed sample.

A comparator (unsealed) hard anodised coating was also examined by visual microscopy and SEM. Free surface and cross-sectional SEMs are shown in Figure 6(a) and 6(b), respectively. Significant porosity is again evident and extends down to the surface in some places. However, from a visual survey the overall level of porosity appears to be somewhat less than in the PEO coating. The porosity and microstructure are also less uniform than for the PEO sample with noticeable cracks of connected porosity. A number of brighter contrast (Si rich) particles were visible within the coating.

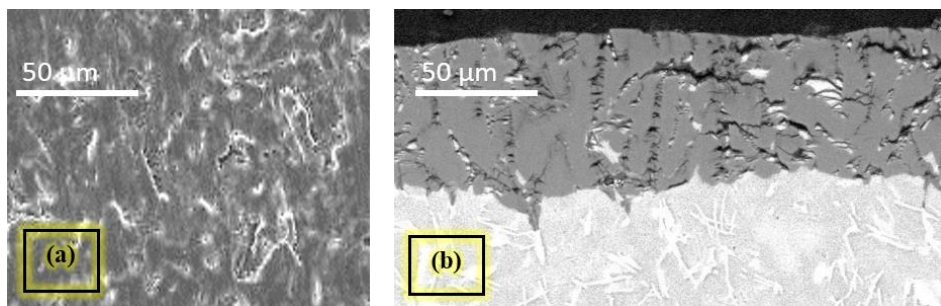


Figure 6 (a) Free surface SEM of a hard-anodised coating, and (b) cross-sectional SEM of the coating.

3.1.2 Thermal property measurements

Laser flash measurements were performed on coupons from room temperature to 400°C. Results for coupon measurements of the optimized coating is shown in Figure 7 below:

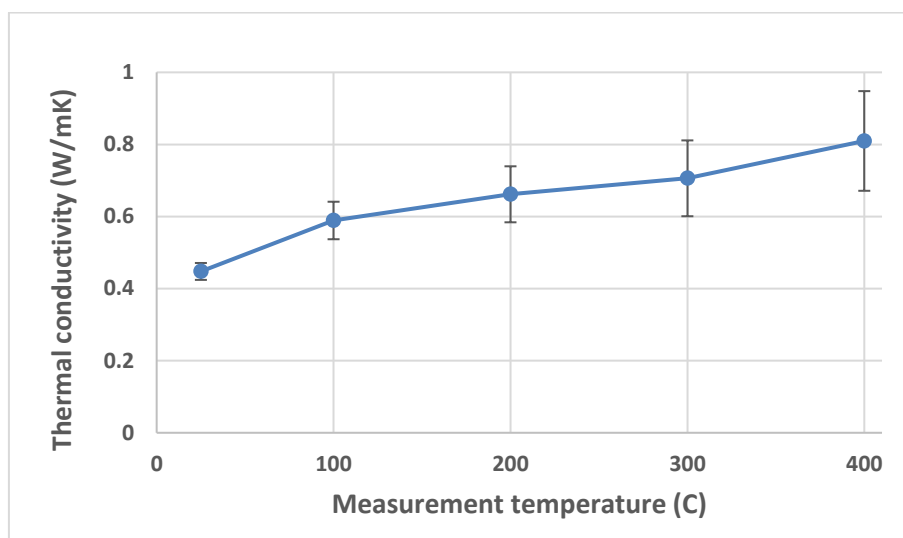


Figure 7 Thermal conductivity of the PEO coating as a function of temperature.

Thermal conductivity is measured to rise from ca. 0.45 W/mK to ca. 0.8 W/mK at 400°C, significantly below that target of 1 W/mK and also below those reported by Toyota for their “SiRPA” coatings [22]. Good reproducibility is seen between samples, especially at lower temperatures (error bars show the standard deviation based on measurement of three samples). This extremely low thermal conductivity derives from two major aspects. Firstly, since air is a poor thermal conductor, the high porosity of the coating results in a significant reduction in the average thermal conductivity versus a fully dense material. Secondly, as discussed above, the coatings incorporate significant quantities of phases such as mullite. These have an intrinsically low thermal conductivity [45].

3.1.3 Piston coating

The optimized coating was applied to the Ford Puma pistons used in this study. Since these were “series” pistons which were pre-treated with a phosphate layer of 1-2 μm , this was removed by an acid etch in dilute nitric acid (pH \sim 1.4) followed by light mechanical abrasion. Coatings were then applied to a nominal coating thickness of 65-70 μm . Following washing and drying a silicate rich sealer (as used on the coupons) was then applied to the coating and cured at 100°C.

Both “PEO-1” and “PEO-4” pistons were coated on the entire top face including the bowl area. Wax masking was used to ensure that no coating was present on the sides of the pistons.

The as-coated surfaces had a Ra of \sim 2.7-2.9 μm . Following application of the sealer the Ra was considerably reduced to \sim 0.7-0.9 μm . For PEO-1 an extra smooth sealer layer was applied to the bowl which gave an Ra of \sim 0.4-0.5 μm . The higher smoothness of the sealer layer on PEO-1 is believed to be due to the sealer thickness being at the higher end of the range (\sim 2 μm) versus being at the lower end of the range (\sim 5 μm) on PEO-4.

3.2 Engine combustion and performance

The in-cylinder pressure traces for different piston coatings, along with the corresponding fuel injection signals, for injection timing A are shown in Figure 8 (other injection timings were omitted due to space limitation, but exhibited similar behavior). It can be seen that the PEO coated pistons, particularly PEO1, demonstrate higher in-cylinder pressure levels relative to the uncoated piston; the increase in maximum cylinder pressure value with PEO1 relative to BSLN is as high as 3% (\pm 1%). This is mainly attributed to the insulation effect of the TBC, where the reduced heat transfer to the cylinder wall increases the average gas temperature and, consequently, pressure [11]. The increased in-cylinder temperature results in a shorter ignition delay and earlier start of combustion, where this leads to attaining the maximum cylinder pressure closer to the TDC, and at higher values too [46].

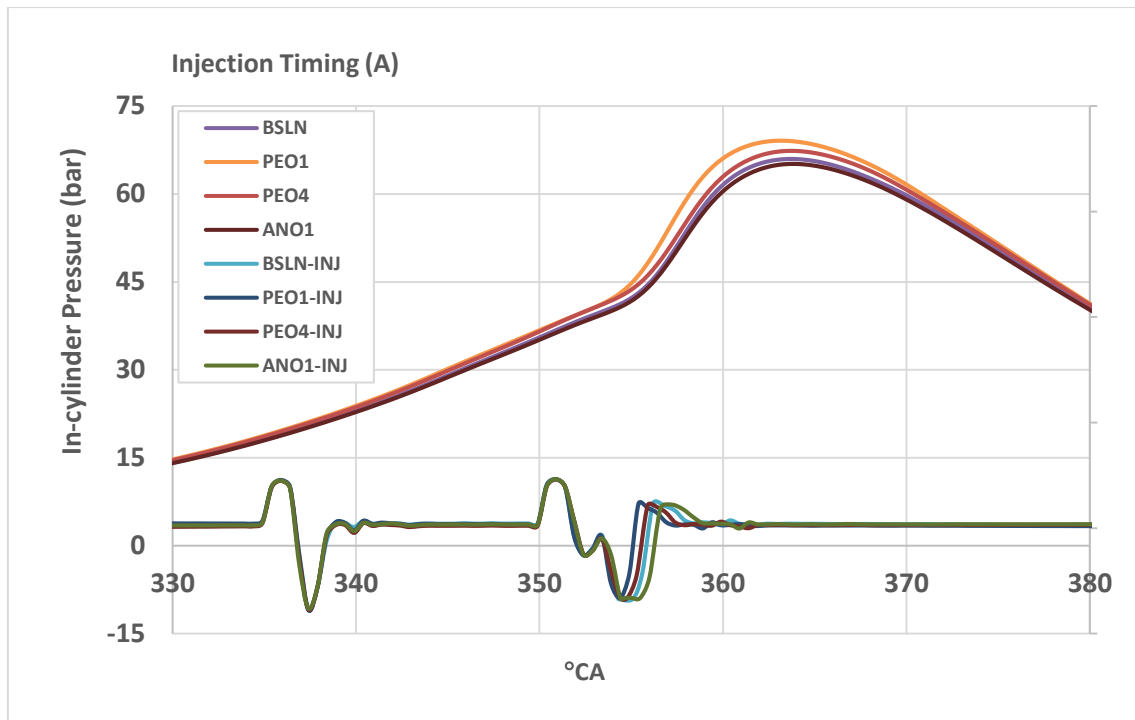


Figure 8 In-cylinder pressure at 1500rpm, 3.8 bar IMEP_n, and corresponding diesel fuel injection signal for injection timing (A).

With reduced heat transfer to the cylinder wall due to the TBC effect, the amount of useful heat that is converted into work acting on the top of the piston increases. The cumulative net heat release (CNHR) for different piston coatings versus the total fuel energy (FE), for injection timing A is shown in Figure 9. By observing the ratio of the CNHR to FE in figure 9, it can be seen that the PEO coatings demonstrate better fuel conversion; a direct consequence of the reduced coolant loss. While the ultimate values of the cumulative HR for all piston coatings are comparable (for the same IMEP_n load conditions), the fuel energy supplied to the engine with PEO coatings was less than those with the BSLN and ANO coating. In comparison with BSLN, PEO1 offers more than 3% increase in the ratio of the cumulative net HR to the fuel energy supplied, as a result of the reduced heat loss; signifying improved engine efficiency [15]. The fuel injection profile, as illustrated by the injector current clamp signal in the figure, demonstrate a slightly shorter duration (i.e. less fuel quantity) for the main injection with the PEO coatings, indicating an improved fuel economy.

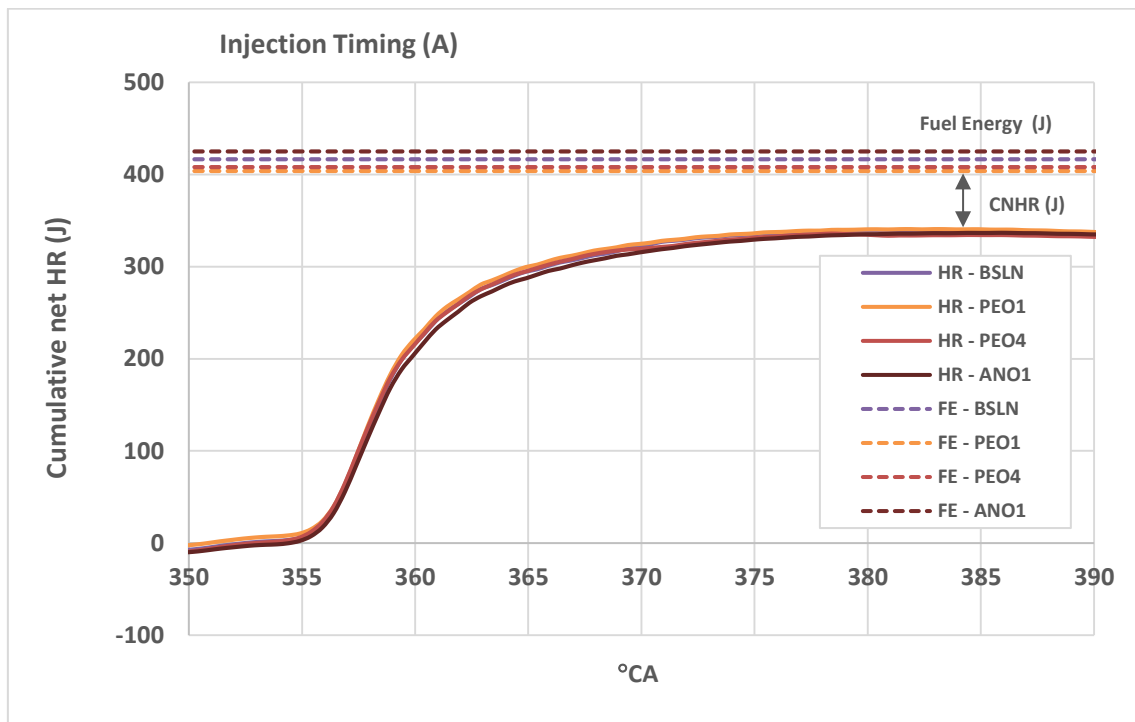


Figure 9 Cumulative net HR data vs total fuel energy at 1500rpm, 3.8 bar IMEPn, for injection timing (A).

Also, higher in-cylinder pressure values imply increased work per cycle transferred into the piston; i.e. indicated work. The gross indicated thermal efficiency trends versus the position of the CA50 dictated by the injection timing, are presented in Figure 10 for different piston coatings. It can be seen that for all coatings, the maximum value of the gross indicated thermal efficiency is achieved where the CA50 is attained at about 8° CA ATDC. Optimum injection timing, therefore, should be selected such that it achieves this point, so as to compromise between power, heat transfer and exhaust gas energy [41]. As far as different coatings are considered, it can be seen that the PEO1 piston demonstrates the highest gross indicated thermal efficiency, at all injection timings, with a maximum increase approaching 3% (absolute) relative to the baseline data. PEO4 also exhibit higher gross indicated thermal efficiency than BSLN despite the comparable in-cylinder pressure values. This is attributed to the improved fuel economy, where less amount of fuel is used to generate the

same load levels. The case is reversed with ANO1, where the increased fuel amount results in lower gross indicated thermal efficiency. The total fuel injection amount (pilot + main) for different piston coatings and different injection timings is shown in Figure 11.

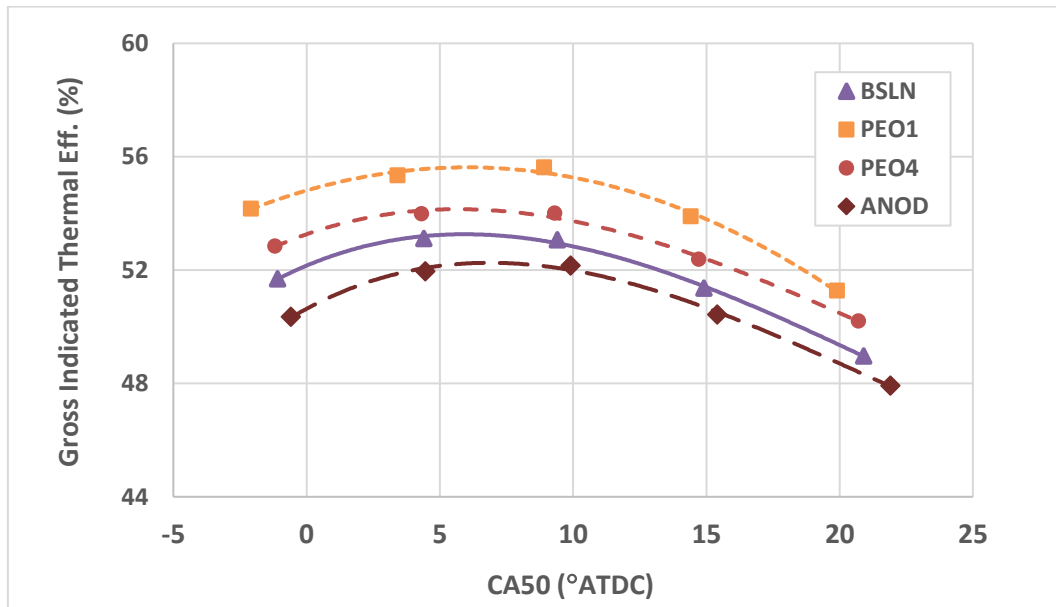


Figure 10 Gross indicated thermal efficiency (%) at 1500rpm, 3.8 bar IMEPn, for different injection timings (as represented by CA50).

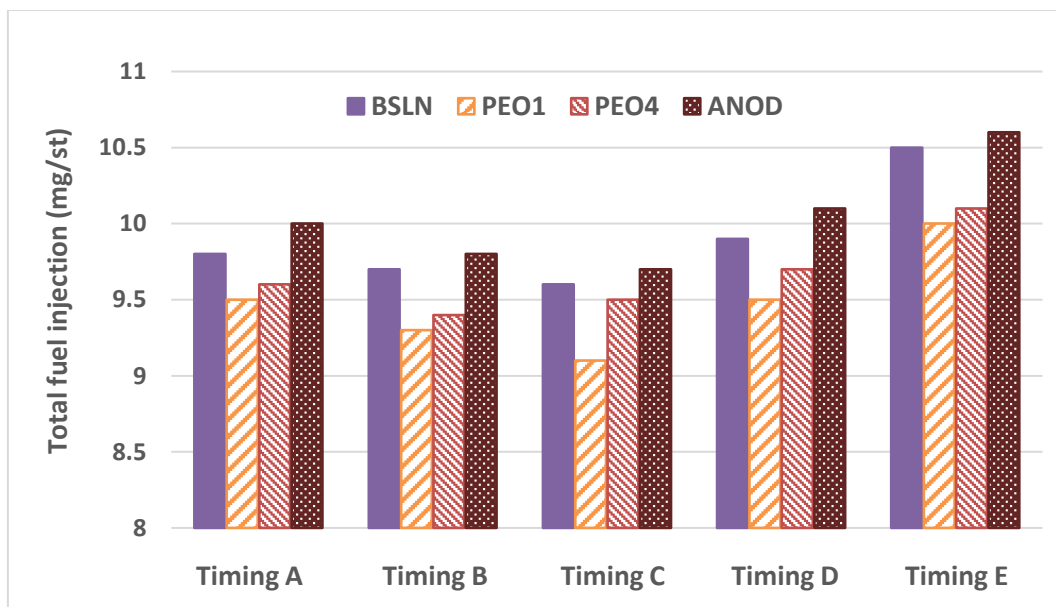


Figure 11 Total fuel injection (mg/st) at 1500rpm, 3.8 bar IMEPn, for different injection timings.

The improvement in the gross indicated thermal efficiency with PEO coatings is fundamentally resulting from the reduced heat loss hence increased work per cycle transferred to the piston. Energy balance for the different piston coatings at injection timing A is presented in Figure 12. Nevertheless, it can be seen that part of the improvement in the gross indicated work is attributed to the reduced exhaust gas losses. From one side, the earlier start of combustion with PEO coatings mean that the exhaust gas will have longer time to expand during the power stroke, hence leaving the cylinder at lower temperature. In addition, the increased charge mass with the BSLN and ANO1 pistons mean the total exhaust mass flow will be larger and at higher temperature, hence the engine suffers more exhaust losses.

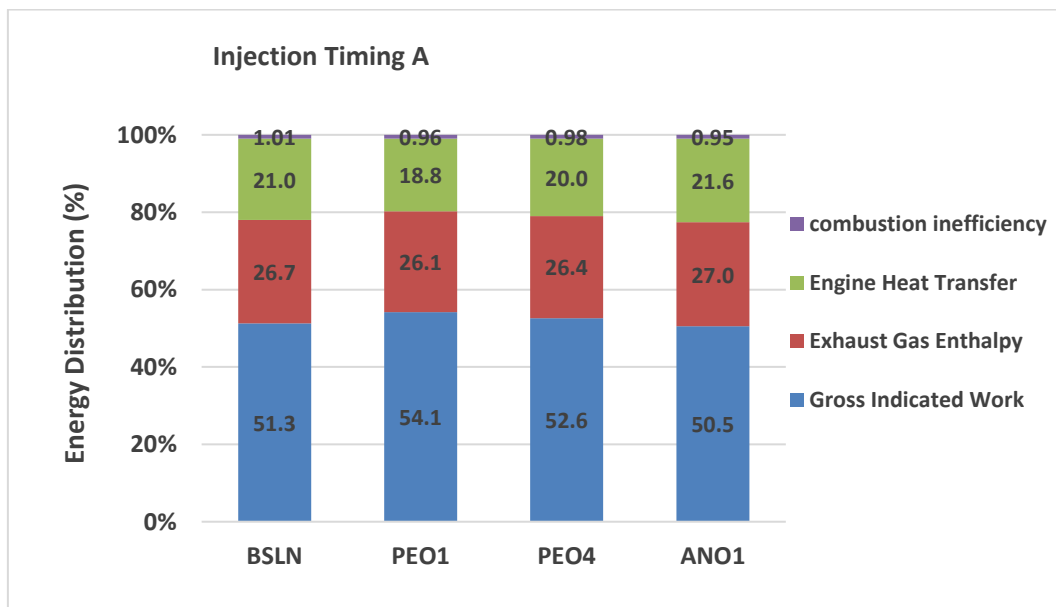


Figure 12 Engine energy balance at 1500rpm, 3.8 bar IMEPn, for different piston coatings, for injection timing A.

3.3 Exhaust emissions

The brake specific NO_x emissions with different piston coatings versus the CA50 are shown in Figure 13. For all pistons, highest NO_x emissions are produced with advanced injection timing, where the ignition delay is longer, the premixed combustion phase is larger, and the peak cylinder pressure is attained closer to the TDC. Accordingly, the peak cylinder temperature is higher; a more favorable conditions for the thermal NO_x formation [10]. As for the piston coatings, it can be seen that PEO1 demonstrates the highest NO_x emissions, at all injection timings. This is due to the elevated cylinder temperature with the reduced heat loss, where the NO_x forms throughout the high temperature burned gases behind the flame front [10]. The increase of NO_x emissions with PEO1 relative to BSLN exceeds 33%. Nevertheless, PEO4 exhibits lower NO_x emissions than BSLN despite the comparable in-cylinder pressure. This could be attributed to the reduced size of the spray cone of the main injection, where the majority of NO_x is formed [47]. The effect is opposite with ANO1, where the rich mixture zone in the fuel spray is larger hence it produces more NO_x relative to BSLN, yet with only marginal increase [48]. It is important to reiterate that no EGR was used during the test, which is typically used to lower NO_x levels in real engines under such operating conditions. This was done deliberately to avoid fluctuations in EGR (rates and temperatures) masking relative differences between coatings.

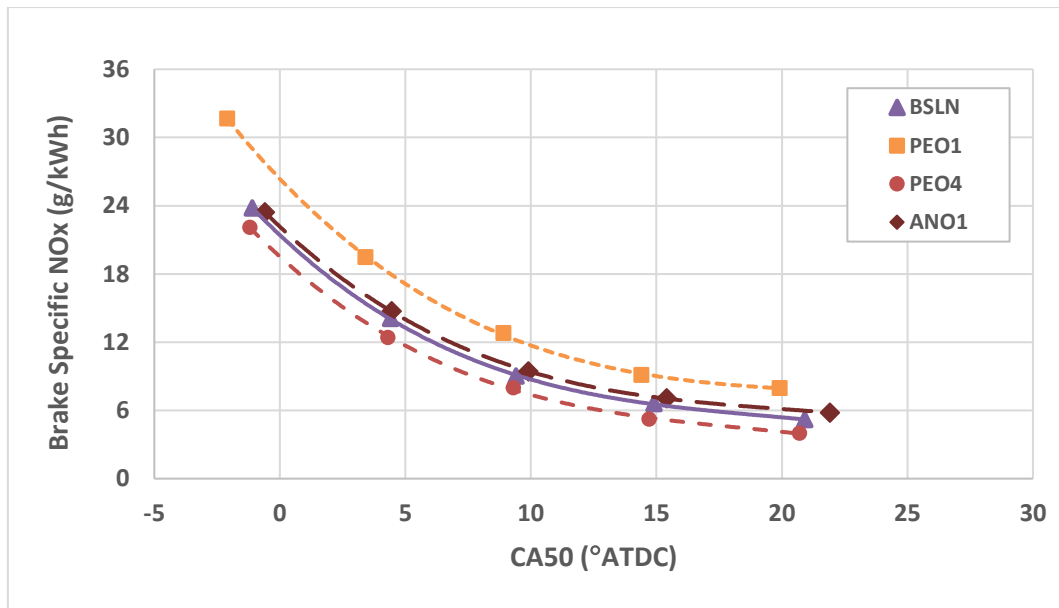


Figure 13 Brake specific NOx emissions at 1500rpm, 3.8 bar IMEPn, for different injection timings (as represented by CA50).

The soot emissions with different piston coatings versus the CA50 are illustrated by Figure 14. The traditional trade-off between NOx and soot is observed with advanced and optimum injection timings; the high temperature combustion with advanced injection timing leads to oxidation of the soot in the flame zone [10]. With the increased diffusion combustion phase as the injection is retarded, soot formation increases. Still, late injection results in increased gas temperature in the late stages of the expansion stroke after the end of diffusion combustion phase, improving soot oxidation [46]. Lowest soot emissions at all injection timings were generated with the PEO1 piston, owing to the high temperature and pressure while the earlier start of combustion offers more residence time for the soot in the high temperature zone, hence promoting oxidation [48]. The reduction of soot emissions with PEO1 relative to BSLN at the optimum injection timing is almost 22%. ANO1 produces lower soot emissions than BSLN, potentially due to the larger volume of the yellow flame zone where the soot oxidation takes place [10].

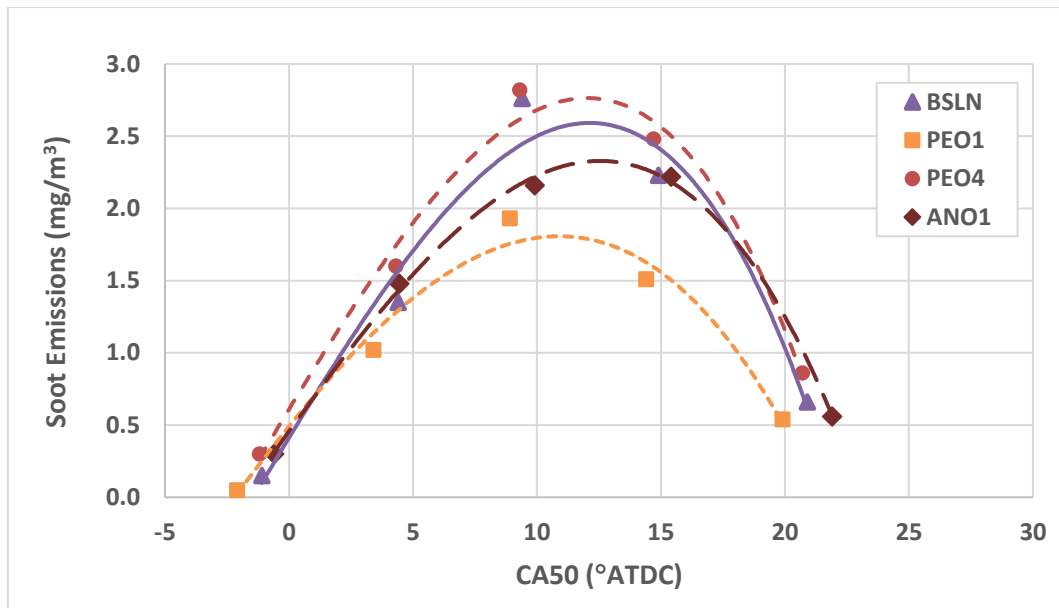


Figure 14 Soot emissions at 1500rpm, 3.8 bar IMEPn, for different injection timings (as represented by CA50).

The brake specific THC emissions with different piston coatings versus CA50 are presented in Figure 15. It can be seen that lowest THC emissions are attained around the optimum injection timing. This is because advanced injection results in a higher cylinder pressure that could push the fuel vapour into the piston crevices hence increase the THC emissions, while retarded injection timing may lead to some of the fuel vapor escaping the combustion process and leave with the exhaust as unburned hydrocarbons [10]. PEO1 demonstrates the lowest THC emissions, due to the high cylinder temperature and the associated better oxidation from one side, and the extra smooth surface finish of the bowl hence no THCs are trapped inside the coating porosities. The reduction of THC emissions with PEO1 relative to BSLN at optimum injection timing exceeds 5%. PEO4, conversely, has regular coating on the bowl where the coating porosities are responsible for tapping some of the unburned hydrocarbon that do not experience combustion, hence increasing the THC emissions. This is analogous to the effect of the presence of porous deposits on the cylinder walls [10]. With ANO1 coating, only the piston crown was coated, so the bowl was free of any porosities that could trap the unburned hydrocarbon hence THC emissions are comparable to those with PEO1.

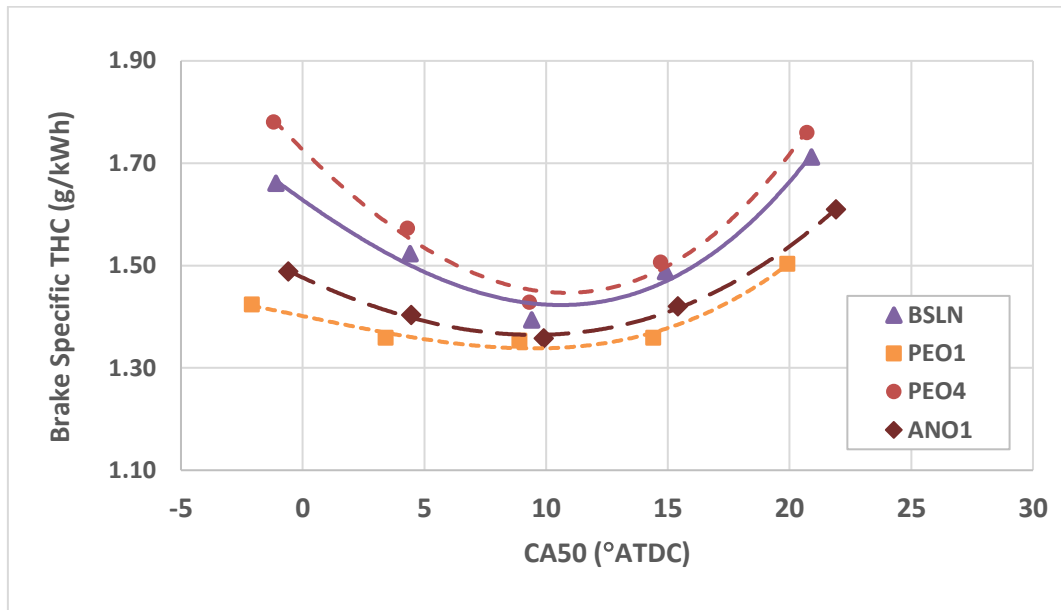


Figure 15 Brake specific THC emissions at 1500rpm, 3.8 bar IMEPn, for different injection timings (as represented by CA50).

The brake specific CO emissions with different piston coatings versus the CA50 are shown in Figure 16. For all piston coatings, the trends of CO emissions are fairly similar to those of THC emissions, where lowest values are mostly obtained with the optimum fuel injection timing. However, PEO1 exhibits comparable CO emissions to those with BSLN, despite the improved oxidation associated with the elevated cylinder temperature. One possible reason for that could partially be the dissociation that occurs in the high-temperature products, even with lean mixtures [10]. As for PEO4, the effect of the nano pores of the bowl coating harboring some of the partially burned products potentially hinders the oxidation of CO, contrary to ANO1 crown-only coating [23].

A detailed analysis of the coatings post-test is beyond the scope of this study. However, while significant soot deposition was evident following the engine tests, it was noted that the coating remained intact and shows good durability under the conditions studied.

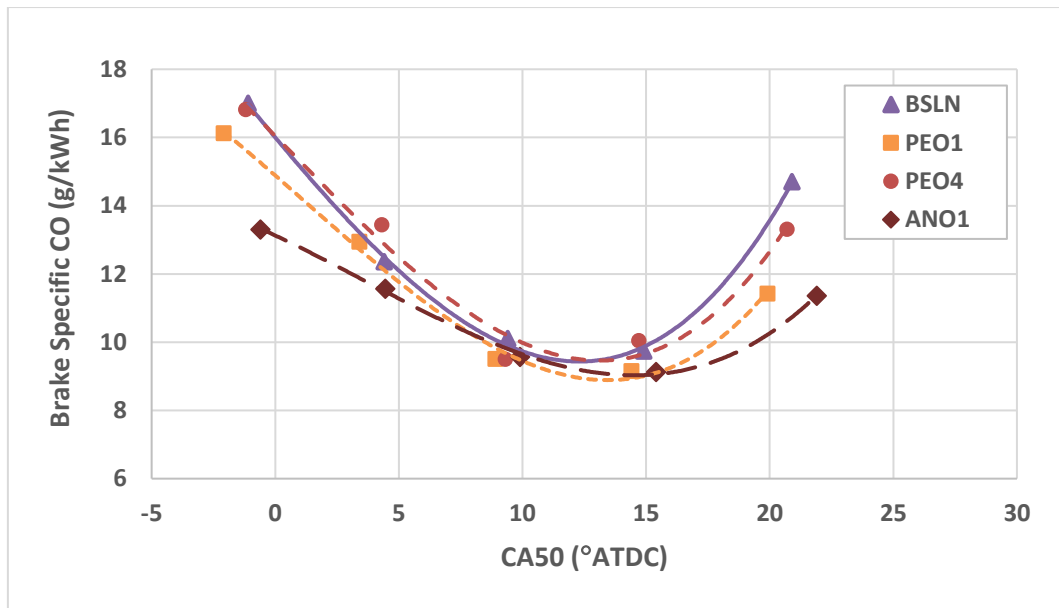


Figure 16 Brake specific CO emissions at 1500rpm, 3.8 bar IMEPn, for different injection timings (as represented by CA50).

4 Conclusions and Future Directions

In this work, the potential benefits of applying a novel PEO coating to an aluminium alloy diesel engine piston were experimentally investigated. Four different pistons were used; a standard uncoated piston (BSLN), a PEO coated piston with an extra smooth surface finish in the bowl (PEO1), an ordinary PEO coated piston (PEO4) and a traditional anodised piston (ANO1). The main findings of the study are:

- PEO is an innovative surface coating technique that overcomes many of the traditional thermal barrier coating methods. It offers an attractive combination of material properties (e.g. hardness, wear resistance, corrosion resistance and interfacial adhesion), on top of effective insulation capabilities. PEO coatings have low thermal conductivities and low heat capacities as needed for thermo-swing coatings. Typical values were found to be around 0.45 w/m.K and 1,500 kJ/m³.K, respectively at room temperature. For the present study, the optimum coating thickness was found to be around 70 μm.

- Under the idealized part load conditions tested, PEO1 demonstrated the best reduction in wall heat transfer losses, with more than 3% gain ($\pm 1\%$) in the fuel useful energy and an equivalent improvement in the indicated thermal efficiency, due to the reduced heat loss to the coolant. Some caution is required when translating this benefit to real multi-cylinder engine operation given the lack of use of EGR in the idealized test (done deliberately to establish relative piston coating effects without unwanted deviations in EGR rate and/or thermodynamic state). PEO4 demonstrated somewhat less good performance than PEO1, but gross indicated thermal efficiency was still significantly above baseline. The anodised comparator piston was found to deliver lower gross indicated thermal efficiency than the baseline.
- Differences in performance between PEO1 and PEO4 may result from differences in surface roughness. For PEO4 a slightly worse surface roughness value was recorded ($R_a \sim 0.7\text{-}0.9 \mu\text{m}$, compared to an R_a of $\sim 0.4\text{-}0.5 \mu\text{m}$ for PEO1). This may result in relative negative interactions of the rougher surface and the gases. However, R_a is only one measure of surface profile and does not measure potential differences in surface “waviness” (e.g. length scales interacting with the local turbulence). These longer length scale features may affect local fuel-air mixing and wall heat transfer, and these effects should be quantified in future work.
- For all piston coatings with the current setup, the optimum injection timing that brings about the best performance, where the CA50 occurs at around 8° CA ATDC, was found to be about -17° CA ATDC for the pilot and -2° CA ATDC for the main fuel injection. Nevertheless, these values are expected to change for different setups and test conditions, hence they should be taken as guidance only.
- Due to the earlier start of combustion and the higher gas temperature, PEO1 exhibits the highest NO_x and lowest soot emissions; the increase of NO_x emissions with PEO1 relative to BSLN exceeds 33%, while the reduction of soot emissions at the optimum injection timing is almost 22%. This increase in NO_x was believed to be indicative of the expected coating thermal effect

during combustion. Retarding the combustion phasing slightly from the optimum would lower NO_x without largely sacrificing the fuel consumption benefit.

- PEO1 demonstrates the lowest THC emissions, due to the high cylinder temperature and the extra smooth surface finish of the bowl that prevents THC trapping within the coating. The reduction of THC emissions with PEO1 relative to BSLN at optimum injection timing exceeds 5%. CO emissions with PEO1 remained comparable to those with BSLN despite the improved oxidation, potentially due to dissociation.
- Future work will extend to consider the thermal interactions of the new coatings with varying EGR effects, other engine surfaces and the potential benefits in advanced gasoline engines (multi-cylinder) with novel fuel injection and combustion systems applicable to future hybrid vehicles.

Acknowledgements

The authors gratefully acknowledge partial funding for the work provided by Innovate UK through the IDP13 programme. The technical support of prior consortium partners is also gratefully acknowledged including Steve Simplay, Steve Whelan and Yogesh Vaidyanathan (all formerly Tata Technologies), Bob Gilchrist and Paul Chandler (formerly JLR) and Tat-Hean Gan, Shila Paul and Ben Robinson (TWI). The authors would also like to extend thanks to Federal Mogul/Tenneco for batch supply of production pistons and Graham Steel from Keronite for support with the laser flash measurements.

References

- [1] Department for Transport. Future of mobility: Urban strategy. March 2019.
- [2] REUTERS. Electric cars win? Britain to ban new petrol and diesel cars from 2040. Available on: <https://uk.reuters.com/article/us-britain-autos-idUKKBN1AB0U5>. (accessed 20 February 2020).
- [3] REUTERS. Electric dream: Britain to ban new petrol and hybrid cars from 2035. Available on: <https://uk.reuters.com/article/us-climate-change-accord-idUKKBN1ZX2RY>. (accessed 20 February 2020).
- [4] International Energy Agency (IEA). Global EV outlook 2019 - Scaling-up the transition to electric mobility. May 2019.
- [5] International Energy Agency (IEA). The Future of trucks – Implications for energy and the environment. 2017.
- [6] Hegab A, La Rocca A, Shayler P. Towards keeping diesel fuel supply and demand in balance: Dual-fuelling of diesel engines with natural gas. *Renewable Sustainable Energy Revs* 2017;70:666-97. <https://doi.org/10.1016/j.rser.2016.11.249>.
- [7] Di Blasio G, Beatrice C, Ianniello R, Pesce FC, Vassallo A, Belgiorno G et al. Balancing hydraulic flow and fuel injection parameters for low-emission and high-efficiency automotive diesel engines. *SAE Tech Pap* 2019-24-0111; 2019. <https://doi.org/10.4271/2019-24-0111>.
- [8] Beatrice C, Di Blasio G, Beatrice C, Belgiorno. Experimental analysis of functional requirements to exceed the 100 kW/l in high-speed light-duty diesel engines. *Fuel* 2017;207:591-601. <http://doi.org/10.1016/j.fuel.2017.06.112>.
- [9] Belgiorno G, Boscolo A, Dileo G, Numidi F, Pesce FC, Vassallo A et al. Experimental study of additive-manufacturing-enabled innovative diesel combustion bowl features for achieving ultra-low emissions and high efficiency. *SAE Tech Pap* 2020-37-0003; 2020. <https://doi.org/10.4271/2020-37-0003>.
- [10] Heywood JB. *Internal combustion engine fundamentals*. New York, USA: McGraw-Hill; 1988.
- [11] Borman G, Nishiwaki k. Internal-combustion engine heat transfer. *Prog Energy Combust Sci* 1987;13(1):1-46. [https://doi.org/10.1016/0360-1285\(87\)90005-0](https://doi.org/10.1016/0360-1285(87)90005-0).
- [12] Kamo R. Adiabatic diesel-engine technology in future transportation. *Energy* 1987;12(10-11):1073-80. [https://doi.org/10.1016/0360-5442\(87\)90063-6](https://doi.org/10.1016/0360-5442(87)90063-6).
- [13] Kamo R. The adiabatic engine for advanced automotive applications. In: Evans RL, editor. *Automotive Engine Alternatives*, New York, USA: Plenum Press; 1987, p. 143-65.

- [14] Woschni G, Spindler W, Kolesa K. Heat Insulation of Combustion Chamber Walls – A Measure to Decrease the Fuel Consumption of I.C. Engines? SAE Tech Pap 8703397; 1987. <https://doi.org/10.4271/870339>.
- [15] Marr MA. An investigation of metal and ceramic thermal barrier coatings in a spark-ignition engine. MASc thesis, Totonto, Canada: Graduate Department of Mechanical and Industrial Engineering, University of Toronto; 2009.
- [16] Arsie I, Cricchio A, Pianese C, Ricciardi V, De Cesare M. Modeling Analysis of Waste Heat Recovery via Thermo-Electric Generator and Electric Turbo-Compound for CO2 Reduction in Automotive SI Engines. Energy Procedia 2015;82:81-8. <https://doi.org/10.1016/j.egypro.2015.11.886>.
- [17] Gao J, Tian G, Sorniotti A, Karci AE, Di Palo R. Review of thermal management of catalytic converters to decrease engine emissions during cold start and warm up. Appl Therm Eng 2019;147:177-87. <https://doi.org/10.1016/j.applthermaleng.2018.10.037>.
- [18] Serrano JR, Arnau FJ, Martin J, Hernandez M, Lombard B. Analysis of engine walls thermal insulation: performance and emissions. SAE Tech Pap 2015-01-1660; 2015. <https://doi.org/10.4271/2015-01-1660>.
- [19] Kumar V. Kandasubramanian B. Processing and design methodologies for advanced and novel thermal barrier coatings for engineering applications. Particuology 2016;27:1-28. <http://doi.org/10.1016/j.partic.2016.01.007>.
- [20] Dhomne S, Mahalle AM. Thermal barrier coating materials for SI engine. J Mater Res Technol 2019;8(1):1532–7. <https://doi.org/10.1016/j.jmrt.2018.08.002>.
- [21] Andrie M, Kokjohn S, Paliwal S, Kamo LS, Kamo A, Procknow D. Low heat capacitance thermal barrier coatings for internal combustion engines. SAE Tech Pap 2019-01-0228; 2019. <https://doi.org/10.4271/2019-01-0228>.
- [22] Wakisaka Y, Inayoshi M, Fukui K, Kosaka H, Hotta Y, Kawaguchi A et al. Reduction of heat loss and improvement of thermal efficiency by application of “temperature swing” insulation to direct-injection diesel engines. SAE Tech Pap 2016-01-0661; 2016. <https://doi.org/10.4271/2016-01-0661>.
- [23] Kawaguchi A, Iguma H, Yamashita H, Takada N, Nishikawa N, Yamashita C et al. Thermo-swing wall insulation technology; - A novel heat loss reduction approach on engine combustion chamber -. SAE Tech Pap 2016-01-2333; 2016. <https://doi.org/10.4271/2016-01-2333>.
- [24] Kikusato A, Terahata K, Jin K, Daisho Y. A numerical simulation study on improving the thermal efficiency of a spark ignited engine --- Part 2: predicting instantaneous combustion

- chamber wall temperatures, heat losses and knock ---. SAE Tech Pap 2014-01-1066; 2014. <https://doi.org/10.4271/2014-01-1066>.
- [25] Caputo S, Millo F, Cifali G, Pesce FC. Numerical investigation on the effects of different thermal insulation strategies for a passenger car diesel engine. SAE Tech Pap 2017-24-0021; 2017. <https://doi.org/10.4271/2017-24-0021>.
- [26] Hoffmam MA, Lawler BJ, G üralp OA, Najt PM, Filipi ZS. The impact of a magnesium zirconate thermal barrier coating on homogeneous charge compression ignition operational variability and the formation of combustion chamber deposits. Int J Engine Res 2015;16(8):968-81. <https://doi.org/10.1177/1468087414561274>.
- [27] Kosaka H, Wakisaka Y, Nomura Y, Hotta Y, Koike M, Nakakita K. Concept of “temperature swing heat insulation” in combustion chamber walls, and appropriate thermo-physical properties for heat insulation coat. SAE Tech Pap 2013-01-0274; 2013. <https://doi.org/10.4271/2013-01-0274>.
- [28] Fukui K, Wakisaka Y, Nishikawa K, Hattori Y, Kosaka H, Kawaguchi A. Development of instantaneous temperature measurement technique for combustion chamber surface and verification of temperature swing concept. SAE Tech Pap 2016-01-0675; 2016. <https://doi.org/10.4271/2016-01-0675>.
- [29] Kogo T, Hamamura Y, Nakatani K, Toda T, Kawaguchi A, Shoji A. High efficiency diesel engine with low heat loss combustion concept - Toyota’s inline 4-cylinder 2.8-liter ESTEC 1GD-FTV engine -. SAE Tech Pap 2016-01-0658; 2016. <https://doi.org/10.4271/2016-01-0658>.
- [30] Somhorst J , Oevermann M, Bovo M, Denbratt I. Evaluation of thermal barrier coatings and surface roughness in a single-cylinder light-duty diesel engine. Int J Engine Res 2019;1-21. <https://doi.org/10.1177/1468087419875837>.
- [31] Kawaguchi A, Wakisaka Y, Nishikawa N. Thermo-swing insulation to reduce heat loss from the combustion chamber wall of a diesel engine. Int J Engine Res 2019;20(7),805-16. <https://doi.org/10.1177/1468087419852013>.
- [32] Caputo S, Millo F, Boccoardo G, Piano A, Cifali G, Pesce FC. Numerical and experimental investigation of a piston thermal barrier coating for an automotive diesel engine application. Appl Therm Eng 2019;162:114233. <https://doi.org/10.1016/j.applthermaleng.2019.114233>.
- [33] Mohedano M, Lu X, Matykina E, Blawert C, Arrabal R, Zheludkevich ML. Plasma electrolytic oxidation (PEO) of metals and alloys. Encycl Interfacial Chem 2018;423-38. <https://doi.org/10.1016/B978-0-12-409547-2.13398-0>.
- [34] Curran JA, Clyne TW. Thermo-physical properties of plasma electrolytic oxide coatings on aluminium. Surf Coat Technol 2005;199:168-76. <https://doi.org/10.1016/j.surfcoat.2004.09.037>.

- [35] Clyne TW, Troughton SC. A review of recent work on discharge characteristics during plasma electrolytic oxidation of various metals. *Int Mater Revs* 2019;64(3):127-62.
<https://doi.org/10.1080/09506608.2018.1466492>.
- [36] Hussein RO, Northwood DO, Nie X. The effect of processing parameters and substrate composition on the corrosion resistance of plasma electrolytic oxidation (PEO) coated magnesium alloys. *Surf Coat Technol* 2013;237:357-68.
<https://doi.org/10.1016/j.surfcoat.2013.09.021>.
- [37] Darband GB, Aliofkhaezrai M, Hamghalam P, Valizade N. Plasma electrolytic oxidation of magnesium and its alloys: Mechanism, properties and applications. *J Magnesium Alloys* 2017;5(1):74-132. <https://doi.org/10.1016/j.jma.2017.02.004>.
- [38] Walsh FC, Low CTJ, Wood RJK, Stevens KT, Archer J, Poeton AR et al. Plasma electrolytic oxidation (PEO) for production of anodised coatings on lightweight metal (Al, Mg, Ti) alloys. *Trans IMF* 2009;(87)3:122-35. <https://doi.org/10.1179/174591908X372482>.
- [39] Min S, Blumm J, Lindemann A. A new laser flash system for measurement of the thermophysical properties. *Thermochim Acta* 2007;455:46-9.
<https://doi.org/10.1016/j.tca.2006.11.026>.
- [40] Abdelaal MM, Hegab AH. Combustion and emission characteristics of a natural gas-fueled diesel engine with EGR. *Energy Convers Manage* 2012;64:301-12.
<https://doi.org/10.1016/j.jma.2017.02.004>.
- [41] de O Carvalho L, de Melo TCC, de Azevedo Cruz Neto RM. Investigation on the fuel and engine parameters that affect the half mass fraction burned (CA50) optimum crank angle. *SAE Tech Pap* 2012-36-0498; 2012. <https://doi.org/10.4271/2012-36-0498>.
- [42] Belgiorno G, Dimitrakopoulos N, Di Blasio G, Beatrice C, Tunestål P, Tunér M. Effect of the engine calibration parameters on gasoline partially premixed combustion performance and emissions compared to conventional diesel combustion in a light-duty Euro 6 engine. *Appl Energy* 2018;228:2221-34. <https://doi.org/10.1016/j.apenergy.2018.07.098>.
- [43] Ladommatos N, Abdelhalim S, Zhao H, The effects of exhaust gas recirculation on diesel combustion and emissions, *Int J Engine Res* 2000;1(1):107-26.
<https://doi.org/10.1243/1468087001545290>.
- [44] Curran JA, Kalkanci H, Magurova Y, Clyne TW. Mullite-rich plasma electrolytic oxide coatings for thermal barrier applications. *Surf Coat Technol* 2007;201:8683-7.
<https://doi.org/10.1016/j.surfcoat.2006.06.050>.

- [45] Kawaguchi A, Tateno M, Yamashita H, Iguma H, Yamashita A, Takada N et al. Heat insulation by “temperature swing” in combustion chamber walls (third report). *Trans Soc Automot Eng Jpn* 2016;47(1):47-53. <https://doi.org/10.11351/jsaeronbun.47.47>.
- [46] Stone R. *Introduction to internal combustion engines*. 3rd ed. Oxford, UK: Macmillan; 1999.
- [47] Turns SR. *An introduction to combustion: Concepts and applications*. 2nd ed. New York, USA: McGraw-Hill; 2000.
- [48] Abdelaal MM, Rabee BA, Hegab AH. Effect of adding oxygen to the intake air on a dual-fuel engine performance, emissions, and knock tendency. *Energy* 2013;61:612-20. <https://doi.org/10.1016/j.energy.2013.09.022>.